


Copyright (2023) Acoustical Society of America. This article may be downloaded for personal use only. Any other use requires prior permission of the author and the Acoustical Society of America. The following article appeared in:

S. D. Bellows et al., “Modeling the sound radiation of gamelan gongs using analytic rigid spherical models”, *Proc. Meet. Acoust.* **51**, 035003 (2023)

and may be found at <https://doi.org/10.1121/2.0001754>

OCTOBER 05 2023

Modeling the sound radiation of gamelan gongs using analytic rigid spherical models **FREE**

Samuel David Bellows ; Micah R. Shepherd; Kent L. Gee ; Timothy W. Leishman



Proc. Mtgs. Acoust. 51, 035003 (2023)

<https://doi.org/10.1121/2.0001754>



View
Online



Export
Citation

CrossMark



LEARN MORE

Advance your science and career as a member of the
Acoustical Society of America



184th Meeting of the Acoustical Society of America

Chicago, Illinois

8-12 May 2023

Musical Acoustics: Paper 4pMUa5

Modeling the sound radiation of gamelan gongs using analytic rigid spherical models

Samuel David Bellows, Micah R. Shepherd, Kent L. Gee and Timothy W. Leishman

Department of Physics and Astronomy, Brigham Young University, Provo, UT, 84602;

samuel.bellows11@gmail.com; micah_shepherd@byu.edu, kentgee@byu.edu, tim.leishman.byu@gmail.com

The structural modes of gamelan gongs have clear connections with the gongs' far-field radiated patterns. However, the instruments' unique geometry and modal characteristics limit the applicability of simple theoretical models, such as a radially vibrating cap on a sphere, for understanding their radiation. This work develops and applies two different models, a vibrating cap on a spherical shell with a circular aperture and a vibrating cap with imposed mode shapes, to better understand the gongs' directional characteristics. The models agree with acoustical measurements, predicting dipole and cardioid-like patterns and lobes formed from constructive and destructive interference.

1. INTRODUCTION

Gongs play an essential musical role in the Balinese and Javanese gamelan. The instruments' construction and tuning processes strongly influence their unique structural and acoustic properties.^{1,2} Several gongs exist within the Balinese gamelan, each with special musical functions related to these properties, such as the strong beating effects evident in the ageng gongs.³ Beyond their unique structural acoustics, the gongs have complex radiation patterns.^{4,5} However, few existing theoretical models can predict the distinctive directional characteristics.

Theoretical models are important tools for understanding directivities. Researchers have employed models such as infinitely baffled flat pistons and their variants,⁶⁻⁹ unbaffled flat pistons,^{6,10} and rigid spheres with vibrating caps¹¹⁻¹³ to better understand sound radiation from loudspeakers,^{6,14,15} the human voice,¹⁶⁻¹⁸ and other sources. For several reasons, gamelan gongs present a unique challenge for these classical models. First, the gongs have a side rim that extends a significant distance behind the gong face, relative to its radius. This structural characteristic forms a cavity-like geometry that breaks the reflectional symmetry about the face plane. Interactions between the gong's face and back opening preclude the use of infinitely baffled models, while the lack of reflectional symmetry limits the applicability of unbaffled flat piston models. Additionally, the directional radiation is highly dependent on the gong's modal response,⁵ meaning effective models must incorporate varying surface velocity distributions. These features limit the utility of commonly applied theoretical models in predicting gamelan gong radiation patterns.

This work presents two theoretical models that help describe the radiation. Both are based on spherical models to avoid the shortcomings of flat pistons and their counterparts. The first is a radially vibrating cap on a rigid spherical shell with a circular aperture. This model is beneficial for understanding how the cavity-like gong geometry influences its directional response. The second model comprises a vibrating cap with imposed mode shapes on a rigid closed sphere. This model explains how varying modal patterns on the gong's surface impact its directivity. Comparisons between modeled and measured directivities highlight the effectiveness of applying these straightforward models to better understand the instrument's radiation characteristics.

2. THEORETICAL MODELS

A. RADIALLY VIBRATING CAP ON A SPHERICAL SHELL WITH A CIRCULAR APERTURE

The gong's rim or circular side wall presents a challenging aspect for modeling the instrument's radiation. The geometry limits the applicability of models incorporating baffled or unbaffled flat plates because it breaks symmetry assumptions about the gong's face. Dissimilar radiation from the gong's front and back interact to create distinctive radiation patterns.

As suggested by Fig. 1, a rough approximation to the gong's geometry is a radially vibrating cap set on a rigid spherical shell with a circular aperture. While this model treats the gong's face as curved rather than flat, it does incorporate the open-back topology. Consequently, this model provides insights into the interactions between the vibrating surface and the open aperture created by the gong's rim.

This geometric configuration requires numerical or semi-analytical approaches for arbitrary frequencies.^{19,20} However, a low-frequency approximation follows by superposing two radially vibrating caps on a rigid sphere. The first cap, oriented toward (ϑ_c, φ_c) and located on the boundary Γ_c , has normal velocity u_c and half angle (i.e., edge angle from center) μ_c . This cap represents the source's radiation if the spherical aperture is closed. The second cap, oriented toward (ϑ_a, φ_a) and located on the boundary Γ_a , has normal velocity u_a and half-angle μ_a . Ensuring the continuity of the spatially averaged pressure and volume velocity across Γ_a will determine this cap's normal velocity.

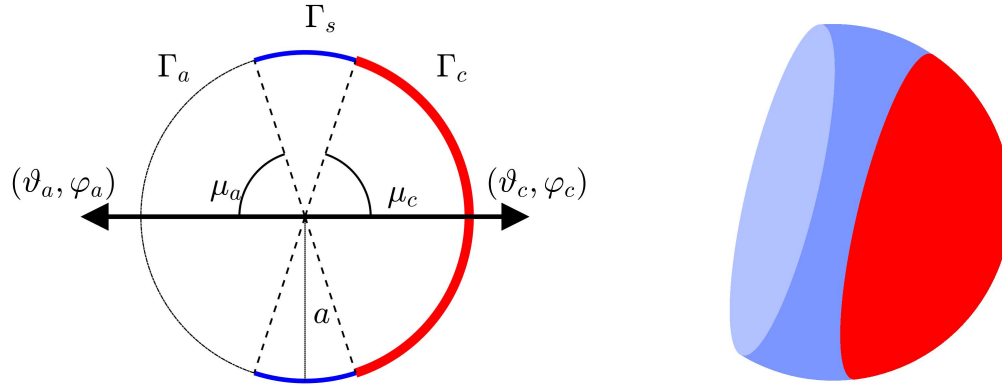


Figure 1: Diagram of a radially vibrating cap on a spherical shell with a circular aperture. The red regions indicate the vibrating portion while the blue regions indicate the rigid portion of the spherical shell.

The pressure produced by a radially vibrating cap on a rigid closed sphere of radius a is^{6,11}

$$p(r, \theta, \phi, k) = -iz_0 \sum_{n=0}^{\infty} \sum_{m=-n}^n U_n^m \frac{h_n^{(2)}(kr)}{h_n^{(2)'}(ka)} Y_n^m(\theta, \phi), \quad r > a, \quad (1)$$

where k is the wavenumber, $z_0 = \rho_0 c$ is the characteristic specific acoustic impedance, $h_n^{(2)}$ are the spherical Hankel functions of the second kind (for $e^{i\omega t}$ time dependence), and Y_n^m are the spherical harmonics of degree n and order m . The sphere's normal surface velocity expansion coefficients U_n^m are

$$U_n^m = u_0 B_n^m(\mu, \vartheta, \varphi), \quad (2)$$

where u_0 is the cap normal velocity, μ is the cap half-angle, and (ϑ, φ) is the direction about which the cap is directed. The coefficients

$$B_n^m(\mu, \vartheta, \varphi) = B_n(\mu) \frac{4\pi}{(2n+1)} [Y_n^m(\vartheta, \varphi)]^* \quad (3)$$

represent the expansion of a unit-amplitude cap of half-angle μ oriented toward (ϑ, φ) and^{6,11}

$$B_n(\mu) = \begin{cases} \frac{1}{2}(1 - \cos \mu), & n = 0 \\ \frac{1}{2}(P_{n-1}(\cos \mu) - P_{n+1}(\cos \mu)), & n > 0 \end{cases}, \quad (4)$$

are the Legendre polynomial expansion coefficients for a unit amplitude cap of half-angle μ oriented toward $(\vartheta, \varphi) = (0^\circ, 0^\circ)$.

Returning to the two-cap superposition model, the pressure produced by the vibrating cap at Γ_c becomes

$$p_c(r, \theta, \phi, k) = -iz_0 \sum_{n=0}^{\infty} \sum_{m=-n}^n u_c B_n^m(\mu_c, \vartheta_c, \varphi_c) \frac{h_n^{(2)}(kr)}{h_n^{(2)'}(ka)} Y_n^m(\theta, \phi), \quad r > a, \quad (5)$$

while the pressure produced by the vibrating aperture cap becomes

$$p_a(r, \theta, \phi, k) = -iz_0 \sum_{n=0}^{\infty} \sum_{m=-n}^n u_a B_n^m(\mu_a, \vartheta_a, \varphi_a) \frac{h_n^{(2)}(kr)}{h_n^{(2)'}(ka)} Y_n^m(\theta, \phi), \quad r > a. \quad (6)$$

For consistency with the measurement orientation presented later, $(\vartheta_c, \varphi_c) = (90^\circ, 0^\circ)$ and $(\vartheta_a, \varphi_a) = (90^\circ, 180^\circ)$ in this work. The gong's geometry determines the cap half-angles μ_c and μ_a . Applying the continuity boundary conditions across the aperture Γ_a yields the aperture normal velocity u_a in terms of known parameters and the total pressure $p_t = p_c + p_a$ of the source configuration.

Solving for the aperture cap velocity u_a requires the spatially averaged pressure jump across Γ_a due to the vibrating cap at Γ_c and the vibrating cap at Γ_a . By letting $U_c = u_c 2\pi a^2 (1 - \cos \mu_c)$ be the volume velocity of the vibrating cap, U_a be the volume velocity of the aperture opening, and $\langle p \rangle_{\Gamma_a}$ be the spatially-averaged pressure over the aperture surface Γ_a for the closed sphere, one finds that these values relate through self and mutual impedances as

$$\langle p \rangle_{\Gamma_a}^{\pm} = U_a Z_{A,aa}^{\pm} + U_c Z_{A,ac}^{\pm}, \quad (7)$$

where $Z_{A,aa}$ is the self impedance of the aperture cap and $Z_{A,ac}$ is the mutual impedance between the aperture and vibrating caps. The \pm symbol indicates that the expression holds for both the exterior (+) and interior (-) sides. The self and mutual impedances are²¹

$$Z_{A,aa} = \frac{-i4\pi a^2 z_0}{S_a^2} \sum_{n=0}^{\infty} \gamma_n^{\pm}(ka) \frac{B_n(\mu_a)^2}{(2n+1)} \quad (8)$$

and

$$Z_{A,ac} = \frac{-i4\pi a^2 z_0}{S_a S_c} \sum_{n=0}^{\infty} (-1)^n \gamma_n^{\pm}(ka) \frac{B_n(\mu_a) B_n(\mu_c)}{(2n+1)}, \quad (9)$$

where

$$\gamma_n^+(ka) = \frac{h_n^{(2)}(ka)}{h_n^{(2)'}(ka)} \quad (10)$$

and

$$\gamma_n^-(ka) = \frac{j_n(ka)}{j_n'(ka)}. \quad (11)$$

Applying continuity of the spatially averaged pressure $\langle p \rangle_{\Gamma_a}^+ = \langle p \rangle_{\Gamma_a}^-$ across the boundary yields

$$U_a = -U_c \frac{(Z_{A,ac}^+ - Z_{A,ac}^-)}{(Z_{A,a}^+ - Z_{A,a}^-)}. \quad (12)$$

Approximating the aperture velocity u_a as a constant so that it relates the aperture volume velocity as $U_a = u_a 2\pi a^2 (1 - \cos \mu_a)$ results in the expression

$$u_a = -\frac{U_c}{2\pi a^2 (1 - \cos \mu_a)} \frac{(Z_{A,ca}^+ - Z_{A,ca}^-)}{(Z_{A,a}^+ - Z_{A,a}^-)}. \quad (13)$$

The superposition of the velocity expansion coefficients for both caps yields

$$A_n^m = \frac{-iz_0}{h_n^{(2)'}(ka)} \frac{4\pi}{(2n+1)} \left\{ u_c B_n(\mu_c) \left[Y_n^m \left(\frac{\pi}{2}, 0 \right) \right]^* + u_a B_n(\mu_a) \left[Y_n^m \left(\frac{\pi}{2}, \pi \right) \right]^* \right\}, \quad (14)$$

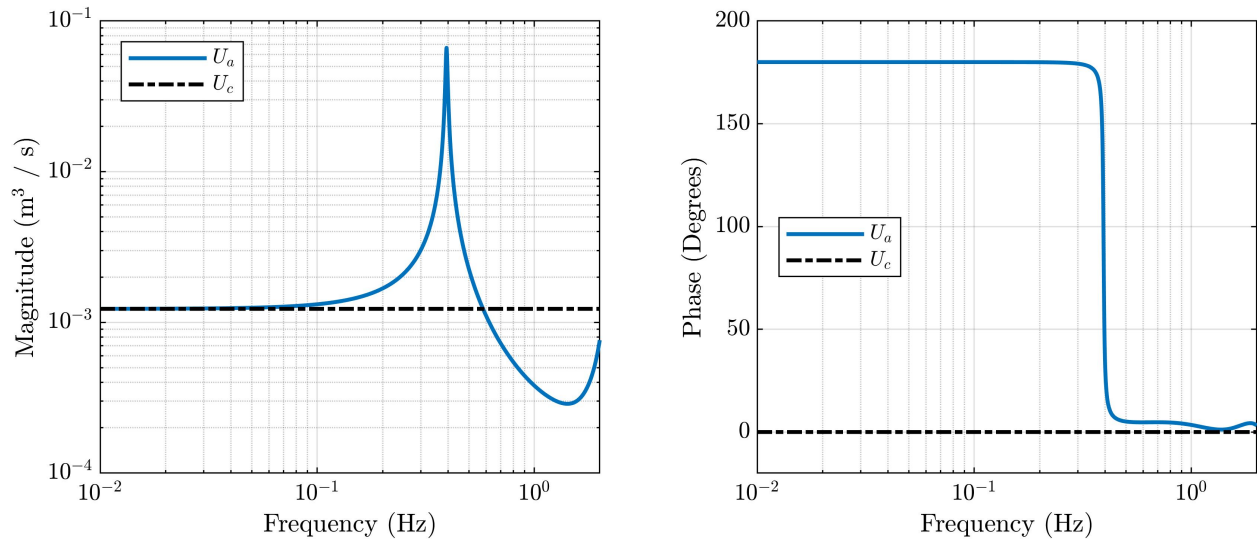


Figure 2: Magnitude and phase of the aperture volume velocity for fixed principal cap volume velocity over frequency.

so that the total pressure is

$$p_t(r, \theta, \phi, k) = \sum_{n=0}^{\infty} \sum_{m=-n}^n A_n^m h_n^{(2)}(kr) Y_n^m(\theta, \phi), \quad r > a. \quad (15)$$

Figure 2 compares the aperture volume velocity U_a to the fixed cap volume velocity U_c as a function of frequency for the case $\mu_c = \mu_a = 18^\circ$ and $a = 1$ m. At low frequencies, the velocity magnitudes are equal but 180° out of phase, which leads to a strong dipole moment.^{10,22} As the frequency approaches the Helmholtz resonance frequency of the cavity, the magnitude of the aperture volume velocity peaks, and the phase changes rapidly from being 180° out of phase to being nearly in phase. Higher volume velocity at the aperture than at the principal cap leads to an increasing monopole moment and omnidirectional radiation at resonance.²² Above the Helmholtz resonance frequency, varying cap and aperture volume velocity ratios can lead to more complex radiation patterns.

Figure 3 plots the normalized far-field directivity of a radially vibrating cap on a rigid spherical shell with a circular aperture having half angles $\mu_c = 45^\circ$ and $\mu_a = 45^\circ$. Balloon color and radius indicate the relative level on a logarithmic scale. Although this model may not be beneficial for representing complex mode shapes, it provides insights into the directional nature of a cavity-like geometry at low frequencies. First, the radiation is primarily dipolar when ka is very small. As ka approaches the Helmholtz resonance frequency of the cavity ($ka \approx 0.7$ for this configuration), the directivity becomes increasingly omnidirectional due to an increasing monopole moment. Above the resonance frequency, the directivity takes on more complex patterns, including cardioid-like radiation. Additionally, radiation behind the aperture is more substantial than in front of the configuration at some frequencies.

B. RADIALLY VIBRATING CAP ON A RIGID SPHERE WITH IMPOSED MODE SHAPES

Varying mode shapes present another challenge for modeling gamelan gong sound radiation. The difficulty of integrating the associated Legendre functions has limited theoretical spherical models to axisymmetric radiation. Although some have contemplated extensions to nonaxisymmetric radiation, the solutions are incomplete or require numerical integration.^{6,12} This section describes a solution for a mode shape imposed on a radially vibrating cap on a rigid sphere.

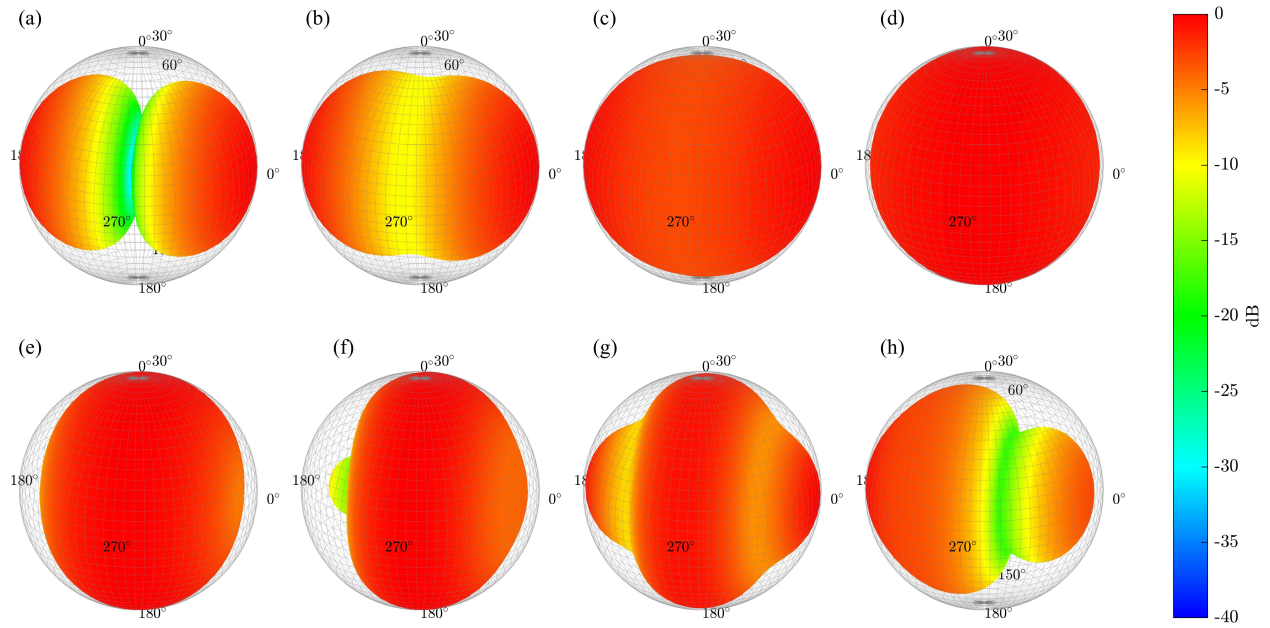


Figure 3: Normalized far-field directivities of a radially vibrating cap on a rigid spherical shell with a circular aperture and 45-degree half angles for (a) $ka = 0.01$, (b) $ka = 0.3$, (c) $ka = 0.6$, (d) $ka = 0.8$, (e) $ka = 1.0$, (f) $ka = 1.5$, (g) $ka = 2.0$, and (h) $ka = 2.5$.

Let μ be the cap half-angle and Ψ_N the desired mode shape. The normal surface velocity is then

$$u_N(\theta, \phi) = \begin{cases} \Psi_N(\theta, \phi) & \theta \leq \mu \\ 0 & \theta > \mu \end{cases}. \quad (16)$$

The spherical harmonic expansion coefficients follow as

$$U_n^m = \int_0^{2\pi} \int_0^\mu \Psi(\theta, \phi) [Y_n^m(\theta, \phi)]^* \sin \theta d\theta d\phi. \quad (17)$$

While the expansion coefficients of Ψ may be difficult to evaluate analytically, consider the simplification of constant-amplitude vibration

$$\tilde{\Psi}(\theta, \phi) = \text{sgn}(\Psi(\theta, \phi)), \quad (18)$$

where sgn is the sign function. Figure 4 demonstrates this operation on the mode shapes of a clamped circular plate. The expansion coefficients of $\tilde{\Psi}$ readily follow by applying spherical-harmonic-domain masking operations.

Consider two functions $f(\theta, \phi)$ and $g(\theta, \phi)$ defined over the sphere with respective spherical harmonic expansion coefficients F_n^m and G_n^m . The expansion coefficients U_n^m of the function $u(\theta, \phi) = f(\theta, \phi)g(\theta, \phi)$ follow from the spatial masking operator as²³

$$H_n^m = \sum_{p=0}^{\infty} \sum_{q=-p}^p \sum_{s=0}^{\infty} \sum_{t=-s}^s \Lambda_{nps}^{mqt} G_p^q F_s^t \quad (19)$$

where

$$\Lambda_{nps}^{mqt} = (-1)^m \sqrt{\frac{(2p+1)(2s+1)(2n+1)}{4\pi}} \begin{pmatrix} p & s & n \\ 0 & 0 & 0 \end{pmatrix} \begin{pmatrix} p & s & n \\ q & t & -m \end{pmatrix} \quad (20)$$

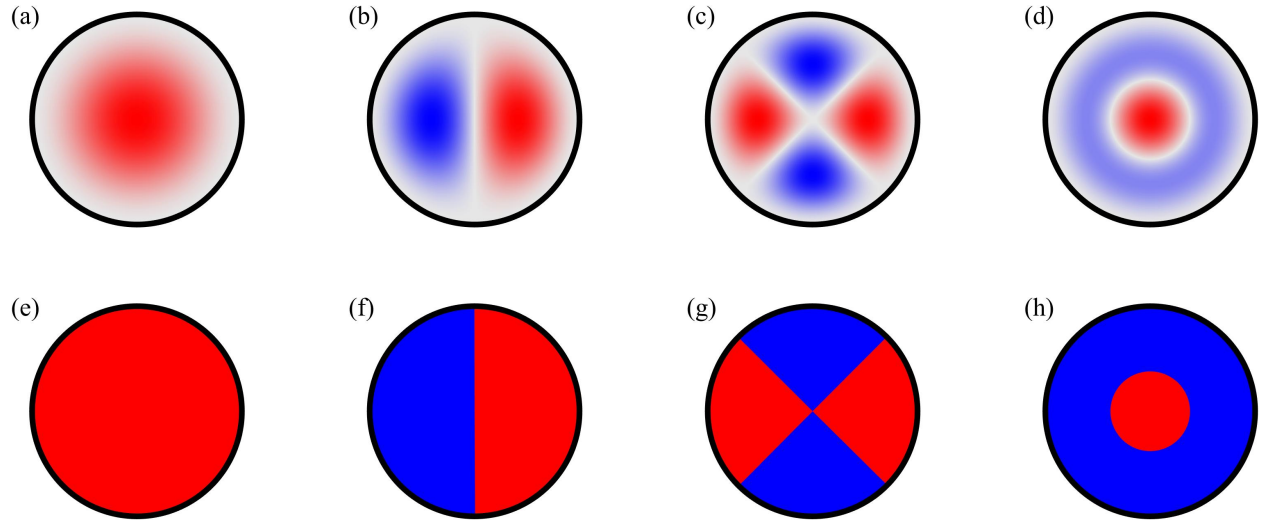


Figure 4: Effects of the sign function on the mode shapes of a clamped circular plate. Mode shapes for (a) $(0,1)$, (b) $(1,1)$, (c) $(2,1)$, and (d) $(0,2)$ modes. Sign function applied to the mode shapes of the (e) $(0,1)$, (f) $(1,1)$, (g) $(2,1)$, and (h) $(0,2)$ modes.

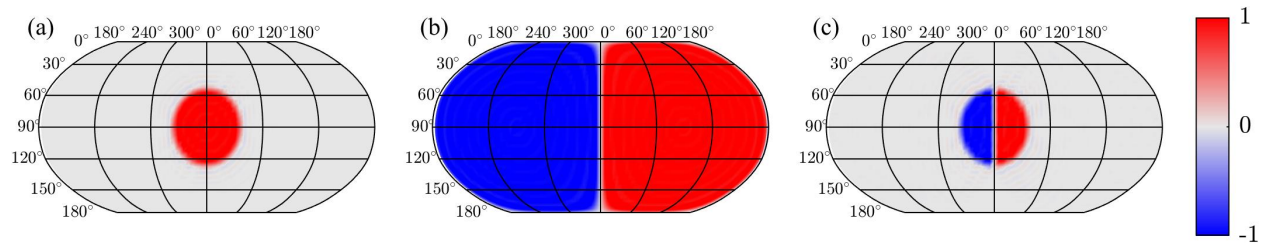


Figure 5: Illustration of using a spatial masking operator to create a $(1,1)$ mode shape. (a) Cap function. (b) Masking function. (c) Expanded result of the spherical-harmonic domain multiplication of the masking and cap functions.

and the matrix-like elements are the Wigner 3j symbols.²³ For practical applications, one may express the masking operator through matrix relations as

$$\mathbf{u} = \mathbf{B}_g \mathbf{f}, \quad (21)$$

where \mathbf{f} and \mathbf{h} are $(N + 1)^2 \times 1$ vectors containing the expansion coefficients truncated to degree N and \mathbf{B}_g is a $(N + 1)^2 \times (N + 1)^2$ matrix containing the operator elements, which depend on the choice of the masking function g . Reference 23 contains more details about this operator, its representation, and its numerical evaluation.

Judicious choices for the functions f and g impose the desired mode shapes onto a spherical cap. For example, Fig. 5 illustrates how one may impose the $(1,1)$ mode shape depicted in Fig. 4 (b) via its simplification shown in Fig. 4 (f) onto spherical a cap with half-angle $\mu = \pi/5$. Choosing $F_n^m = B_n^m(\pi/5, \pi/2, 0)$ produces a spherical cap of half-angle $\mu = \pi/5$ oriented along the x -axis as depicted in Fig. 5(a). Next, choosing the masking function $G_n^m = B_n^m(\pi, \pi/2, \pi/2) - B_n^m(\pi, \pi/2, 3\pi/2)$ divides the spherical surface into two positive and negative constant-amplitude regions as shown in Fig. 5(b). Finally, spherical-harmonic domain multiplication yields the desired surface velocity depicted in Fig. 5(c).

3. RESULTS

A. VIBRATING CAP ON A SPHERICAL SHELL WITH CIRCULAR APERTURE

A spherical model of the gong's radiation requires an estimate of the source's equivalent radius a_e and cap half-angle μ . For a gong with face radius R and wall rim depth d , the equivalent cap half angle μ is

$$\mu \approx \tan^{-1} \left(\frac{2R}{d} \right). \quad (22)$$

The effective radius is more challenging. One could choose $a_e = R$ or $a_e = d/2$, but these choices underestimate and overestimate the cavity volume, respectively. A poor estimate of the cavity volume gives an incorrect prediction of the Helmholtz resonance frequency, degrading the accuracy of the model's predictions. An effective radius $a_e = (3/4R^2d)^{1/3}$ based on a sphere with equivalent volume produced better agreement, but ad hoc experimentation with various combinations of these three approaches determined that an estimate based on

$$a_e = \frac{1}{2} \left[\frac{d}{2} + \left(\frac{3}{4}R^2d \right)^{1/3} \right] \quad (23)$$

yielded the best agreement between predicted and measured directivity results for two gongs.

Figure 6 compares two pairs of measured and modeled gamelan gong radiation patterns for the ageng lanang gong ($R = 0.41$ m, $d = 0.24$ m, $a_e = 0.216$ m, $\mu = 73.7^\circ$). Reference 5 contains more details about the measurement and data processing methods. Figures 6(a) and (c) show results for the $(0, 1)$ axisymmetric mode at 63 Hz. The radiation appears dipole-like, although, as in Fig. 3(b), it is in transition between a dipole-like and monopole-like pattern. The directivity becomes less dipole-like for the $(0, 2)$ mode at 130 Hz, as shown in Figs. 6(b) and (d). Although the $(0, 2)$ mode has two anti-nodal regions that vibrate out-of-phase with each other, the model's prediction remains robust.

Figure 7 compares measured and modeled gamelan gong radiation patterns for the bebende gong ($R = 0.25$ m, $d = 0.175$ m, $a_e = 0.145$ m, $\mu = 70.5^\circ$). Figures 7(a) and 7(c) shows the results for the $(0, 1)$ axisymmetric mode at 144 Hz. As for the ageng lanang gong, the radiation is roughly dipole-like. However, in contrast to the ageng lanang gong, the radiation appears more omnidirectional for the $(0, 2)$ mode at 469 Hz, as shown in Figs. 7(b) and (d). These differences in directivity patterns partly result from differing acoustic wavelengths relative to structural wavelengths. For the ageng lanang gong, the modal frequency spacing is nearly a factor of two, leading to a beating phenomenon following a gong strike.³ In contrast, the modal frequency spacing for the bebende gong is closer to a factor of three. This greater spacing appears to place the modal frequency of the $(0, 2)$ mode closer to the Helmholtz resonance of the gong's cavity and leads to more omnidirectional radiation.

The agreement between the measured and predicted directivities highlights the utility of applying simple theoretical models to better understand radiation behavior. Typical models without an open cavity geometry predict increasing directivity with increasing frequency.^{6,11} In contrast, the proposed spherical model predicts dipolar radiation at the lowest frequencies and *decreasing* directivity as frequency approaches the Helmholtz resonance frequency of the cavity. These theoretical predictions explain why directivities for the $(0, 2)$ modes are *less* directional than the $(0, 1)$ modes.

B. SPHERICAL CAP WITH IMPOSED MODE SHAPES

Figure 8 plots several comparative results for the ageng lanang gong and the spherical cap model with imposed mode shapes. Figures 8(a)-(d) show four selected normal surface velocity distributions based on scanning laser Doppler vibrometer (SLDV) scans of the gong's face.⁵ Figure 8(e)-(g) show the measured directivity patterns at associated spectral peaks, extrapolated to the far-field.⁵ Finally, Figs. 8(h)-(l) show

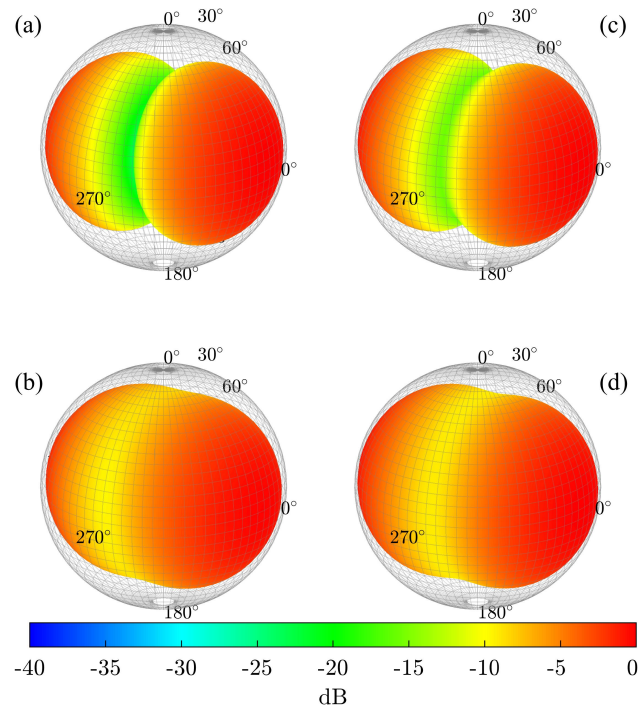


Figure 6: Measured (a)-(b) and modeled (c)-(d) far-field ageng lanang gong directivity results for the (a) and (c) (0,1) mode (63 Hz) and (b) and (d) (0, 2) mode (130 Hz).

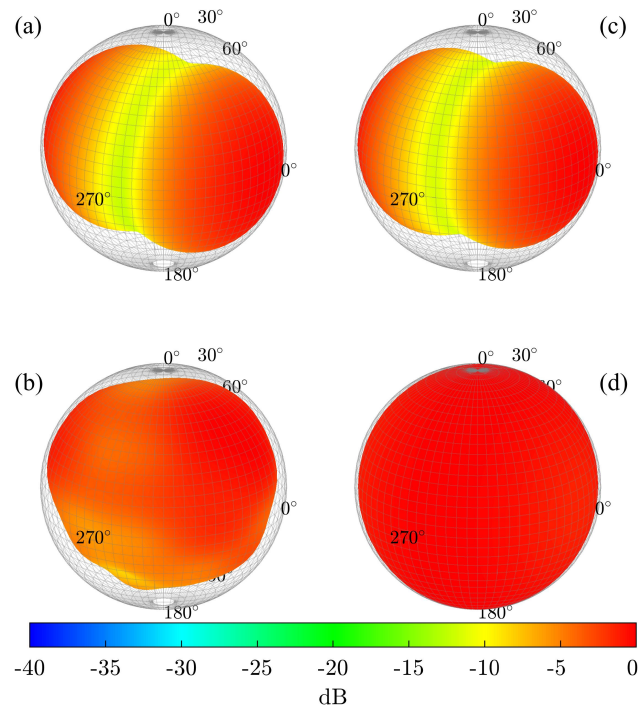


Figure 7: Measured (a)-(b) and modeled (c)-(d) far-field bebende gong directivity results for the (a) and (c) (0,1) mode (144 Hz) and (b) and (d) (0, 2) mode (469 Hz).

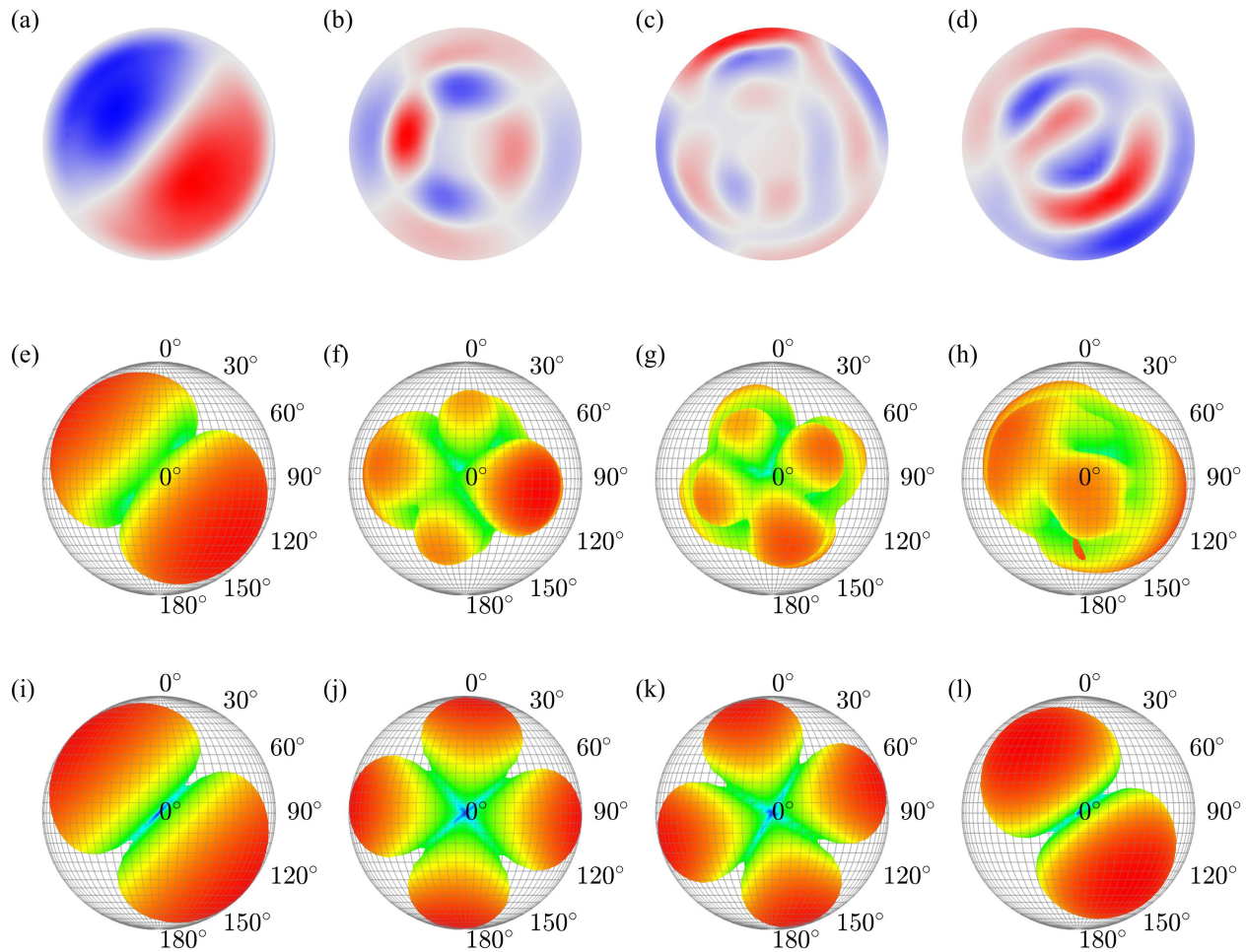


Figure 8: The SLDV out-of-plane surface velocity distributions of the ageng lanang gong measured at (a) 104 Hz, (b) 376 Hz (c) 566 Hz, and (d) 498 Hz. Measured directivities extrapolated to the far-field at (e) 104 Hz, (f) 376 Hz (g) 566 Hz, and (h) 501 Hz. Modeled directivities at (i) 104 Hz, (j) 376 Hz (k) 566 Hz, and (l) 501 Hz.

predicted directivities based on the theoretical model. Although the model employs several simplifying assumptions, it achieves reasonable agreement, particularly at lower frequencies. The directivity results for the (1, 1) mode at 104 Hz shown in Figs. 8 (e) and (i) reveal only slight differences between the measured and predicted values. However, while the theoretical model is highly symmetric and exactly aligned with the x -axis, the measured directivity shows minor asymmetries and some misalignment. These differences could result from inhomogeneities in the gong's construction.

The measured directivity results at 376 Hz and 566 Hz [Figs. 8(f) and (g)] both show four-lobed patterns—even though the associated gong surface velocity distributions differ substantially. The lobe locations and pattern orientations align with the four anti-nodal vibration regions at the gong's edge. Unlike the predicted directivities [Figs. 8(j) and (k)], which exhibit perfect symmetries, the measured results, similar to the (1, 1) mode, have asymmetries. Nonetheless, the predicted directivities also have four-lobe patterns with orientations similar to those of the measured results. This agreement illustrates the utility of simple theoretical models for clarifying directional behaviors.

The measured directivity at 501 Hz seen in Fig. 8(d) shows substantial radiation behind the instrument, although there also appear roughly four lobes, two in front of and two behind the gong. In contrast, the pre-

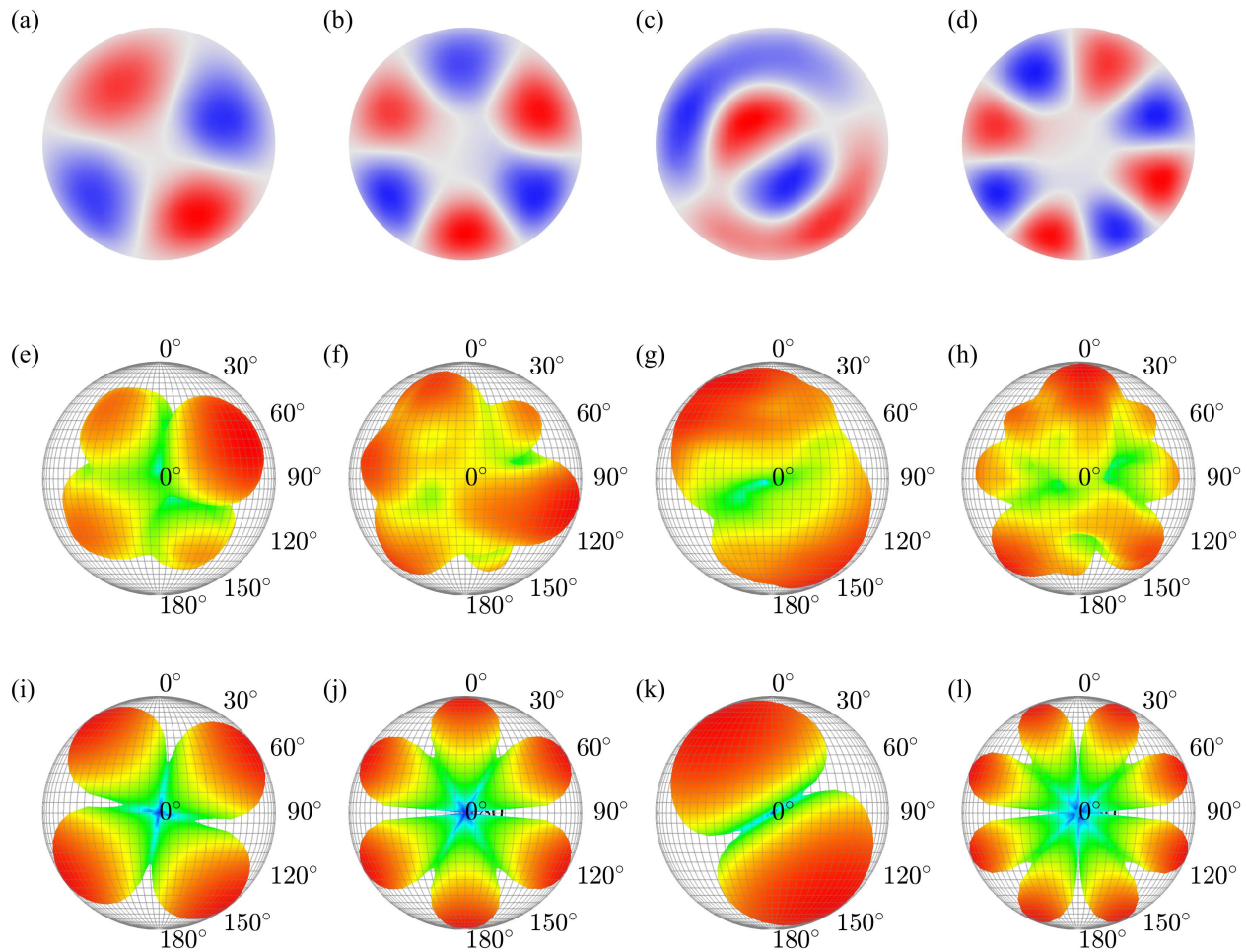


Figure 9: The SLDV out-of-plane surface velocity distributions of the bebende gong measured at (a) 388 Hz (b) 546 Hz (c) 606 Hz (d) 692 Hz. Measured directivities extrapolated to the far-field at (e) 389 Hz (f) 539 Hz (g) 606 Hz (h) 692 Hz. Modeled directivities at (i) 389 Hz (j) 539 Hz (k) 606 Hz (l) 692 Hz.

dicted directivity [Fig. 8(l)] only shows two symmetric lobes. Because the imposed mode shape model does not incorporate the cavity geometry used in the spherical shell model, it cannot predict stronger radiation behind the gong.

Results from the bebende gong further illustrate the model's utility while underscoring its limitations. Figures 9 (a)-(d) show four selected normal surface velocity distributions based on SLDV scans of the gong's face.⁵ Figures 9(e)-(g) show the measured directivity patterns at the associated spectral peaks, extrapolated to the far field. Finally, Figs. 9(h)-(l) show predicted directivities based on the theoretical model. In all four cases, the number of lobes and their relative positions correspond with anti-nodal edge regions of the gong's measured surface velocity. While the measured directivity patterns show similarities in the numbers and orientations of the directional lobes, they exhibit significant asymmetries.

At 389 Hz [Figs. 9(e) and (i)] and 606 Hz [Figs. 9(g) and (k)], the directivity asymmetries are less pronounced, so that the correspondence between the predicted and measured results remains clear. However, the directivities at 539 Hz [Figs. 9(f) and (j)] and 692 Hz [Figs. 9(h) and (l)] show significantly stronger asymmetries. At 539 Hz [Fig. 9(f)] four of the six lobes are very pronounced, while at 692 Hz [Fig. 9(h)], three of the eight lobes are very pronounced. Thus, while the theoretical model shows promise at accurately predicting the numbers and locations of the radiation lobes, neglecting the gong's material and structural

inhomogeneities and other properties limits its efficacy.

4. CONCLUSIONS

This work has presented two theoretical spherical models to study the directional radiation characteristics of gamelan gongs. Both models allow analytic solutions for their far-field radiation. The first is a vibrating cap on a spherical shell with a circular aperture that provides insight into the impacts of the cavity-like geometries on gong radiation. This model predicts dipole radiation at very low frequencies, decreasing directionality approaching the Helmholtz resonance frequency of the cavity and omnidirectional radiation at the resonance frequency. Comparisons of directivities of the axisymmetric modes of two gongs confirmed the model's basic theoretical assertions. The second model is a vibrating cap on a rigid sphere with imposed mode shapes. Comparisons between measured and predicted directivities validated the model's utility in predicting the numbers and locations of directional lobes.

Limitations to the models include their failure to predict the asymmetries present in measured directivities. Future work could combine the models into a single form to incorporate complex mode shapes and cavity geometries. Other models based on cylindrical geometries would also benefit studies of sound radiation from gamelan gongs.

ACKNOWLEDGMENTS

The William James and Charlene Fuhrman Strong Family Musical Acoustics Endowed Fellowship Fund supported S.D.B. during the research and writing. The authors express appreciation for this funding and to Joseph Avila for assistance with the measurements.

REFERENCES

- ¹ N. McLachlan, "Finite element analysis and gong acoustics," *Acoustics Australia*, vol. 25, no. 3, p. 103–107, 1997.
- ² R. Perrin, D. P. Elford, L. Chalmers, G. M. Swallowe, T. R. Moore, S. Hamdan, and B. J. Halkon, "Normal modes of a small gamelan gong," *J. Acout. Soc. Am.*, vol. 136, no. 4, pp. 1942–1950, 2014.
- ³ D. W. Krueger, K. L. Gee, and J. Grimshaw, "Acoustical and vibrometry analysis of a large balinese gamelan gong," *J. Acout. Soc. Am.*, vol. 128, no. 1, pp. EL8–EL13, 2010.
- ⁴ F. Zotter, "Analysis and synthesis of sound-radiation with spherical arrays," *Doctoral Dissertation, Institute of Electronic Music and Acoustics University of Music and Performing Arts*, 2009.
- ⁵ S. D. Bellows, D. T. Harwood, K. L. Gee, and T. W. Leishman, "Low-frequency directional characteristics of a gamelan gong," *Proc. Mtgs. Acoust.*, vol. 50, no. 1, p. 035003, 2022.
- ⁶ L. Beranek and T. Mellow, *Acoustics: Sound fields, transducers and vibration*. Academic Press, 2 ed., 2019.
- ⁷ T. Mellow, "On the sound field of a resilient disk in an infinite baffle," *J. Acout. Soc. Am.*, vol. 120, no. 1, pp. 90–101, 2006.
- ⁸ R. M. Aarts and A. J. E. M. Janssen, "On-axis and far-field sound radiation from resilient flat and dome-shaped radiators," *J. Acout. Soc. Am.*, vol. 125, no. 3, pp. 1444–1455, 2009.

-
- ⁹ M. Greenspan, “Piston radiator: Some extensions of the theory,” *J. Acoust. Soc. Am.*, vol. 65, p. 608, 1979.
- ¹⁰ A. D. Pierce, *Acoustics*. Springer International Publishing, 2019.
- ¹¹ P. M. Morse and K. U. Ingard, *Theoretical Acoustics*. Princeton University Press, 1968.
- ¹² R. M. Aarts and A. J. E. M. Janssen, “Sound radiation from a resilient spherical cap on a rigid sphere,” *J. Acoust. Soc. Am.*, vol. 127, no. 4, pp. 2262–2273, 2010.
- ¹³ C. C. Gerding and W. Thompson, “Axisymmetric spherical radiator with mixed boundary conditions,” *J. Acoust. Soc. Am.*, vol. 61, no. 2, pp. 313–317, 1977.
- ¹⁴ T. Hélie and X. Rodet, “Radiation of a pulsating portion of a sphere: Application to horn radiation,” *Acta Acustica united with Acustica*, vol. 89, no. 4, pp. 565–577, 2003.
- ¹⁵ R. M. Aarts and A. J. E. M. Janssen, “Comparing sound radiation from a loudspeaker with that from a flexible spherical cap on a rigid sphere,” *J. Audio Eng. Soc.*, vol. 59, no. 4, pp. 201–212, 2011.
- ¹⁶ J. L. Flanagan, “Analog measurements of sound radiation from the mouth,” *J. Acoust. Soc. Am.*, vol. 32, no. 12, pp. 1613–1620, 1960.
- ¹⁷ T. Halkosaari, M. Vaalgamaa, and M. Karjalainen, “Directivity of artificial and human speech,” *J. Audio Eng. Soc.*, vol. 53, no. 7/8, pp. 620–631, 2005.
- ¹⁸ T. W. Leishman, S. D. Bellows, C. M. Pincock, and J. K. Whiting, “High-resolution spherical directivity of live speech from a multiple-capture transfer function method,” *J. Acoust. Soc. Am.*, vol. 149, no. 3, pp. 1507–1523, 2021.
- ¹⁹ J. W. Miles, “Scattering by a spherical cap,” *J. Acoust. Soc. Am.*, vol. 50, no. 3B, pp. 892–903, 1971.
- ²⁰ G. Elias and P. Malbéqui, “Scattering by an open sphere: Exact solution and comparison with a boundary integral method,” *J. Acoust. Soc. Am.*, vol. 93, no. 2, pp. 609–616, 1993.
- ²¹ C. H. Sherman, “Mutual radiation impedance of sources on a sphere,” *J. Acoust. Soc. Am.*, vol. 31, no. 7, pp. 947–952, 1959.
- ²² G. Weinreich, “Sound hole sum rule and the dipole moment of the violin,” *J. Acoust. Soc. Am.*, vol. 77, no. 2, pp. 710–718, 1985.
- ²³ R. Kennedy and P. Sadeghi, *Hilbert Space Methods in Signal Processing*. Cambridge University Press, 2013.